On the Modeling of Conducting Media With the Unconditionally Stable ADI–FDTD Method

Chenghao Yuan, *Student Member, IEEE*, and Zhizhang (David) Chen, *Senior Member, IEEE*

***Abstract*—The Courant–Friedrich–Levy stability condition has prevented the conventional finite-difference time-domain (FDTD) method from being effectively applied to conductive materials because of the fine mesh required for the conducting regions. In this paper, the recently developed unconditionally stable alternating-direction-implicit (ADI) FDTD is employed because of its capability in handling a fine mesh with a relatively large time step. The results show that the unconditionally alternating-direction-implicit–finite-difference time-domain (ADI–FDTD) method can be used as an effective universal tool in modeling a medium regardless of its conductivity. In addition, the unsplit perfectly matched layer combined with the ADI–FDTD method is implemented in the cylindrical coordinates and is proven to be very effective even with the cylindrical structures that contain open conducting media.**

***Index Terms*—Alternating-direction-implicit–finite-difference time-domain (ADI–FDTD) method, highly conductive materials, perfectly matched layer (PML).**

I. Introduction

MANY numerical techniques have been developed to model and simulate RF, microwave, and optical circuits and components. In particular, finite-difference time-domain (FDTD) algorithms have been shown thus far to be the powerful tools to predict RF wave behaviors in various circuit media [1], except for the highly conductive materials. In a highly conductive medium, due to the skin effect, a very fine mesh is required to account for the rapidly changing fields. Such a fine mesh leads to a small cell size, which, in turn, forces the time step to be small because of the Courant–Friedrich–Levy stability (CFL) condition. In a normal circumstance at a microwave frequency, the time step is so small that it makes the number of FDTD iterations very large even for simulation of one cycle of a microwave signal. Consequently, effective schemes need to be developed for modeling of highly conductive materials.

Approximate methods, such as the surface impedance boundary condition (SIBC) method and perturbation technique, have been used, as described in [1]. These approximations, however, normally come with assumptions that may lead to errors or even failure in some applications. For instance, SIBC assumes a plane incident wave, which is not true for cylindrical structures. In addition, information on field behaviors inside highly conductive materials is lost because of the use of the surface impedance.

Manuscript received September 11, 2002; revised March 10, 2003. This work was supported by the National Science and Engineering Research Council of Canada.

The authors are with the Department of Electrical and Computer Engineering, DalTech, Dalhousie University, Halifax, NS, Canada B3J2X4 (e-mail: z.chen@dal.ca; cyuan@dal.ca).

Digital Object Identifier 10.1109/TMTT.2003.815267

The recently developed three-dimensional unconditionally stable ADI–FDTD method [2]–[4] presents a possibility in resolving the difficulty. Since the method can go with an arbitrary time step without a stability problem, it can be applied to a fine mesh with a much larger time step. The number of iterations can thus be reduced to a manageable level. The past applications of the ADI–FDTD to thin shielding conductors at low frequencies [5] and to high-Q cavities [6] have demonstrated that the ADI–FDTD method is efficient and effective when a highly graded mesh is required. The corollary presented in [4] has provided a theoretical foundation for the feasibility of such ADI–FDTD applications.

Another issue with the ADI–FDTD is the incorporation of the perfectly matched layer (PML) schemes. Although work has been done in implementing the split PML and complex frequency-shifted (CFS) constitutive PML with the ADI–FDTD [7], [8], no actual testing and experiments were performed for highly conductive media, as well as for nonrectangular coordinates.

In this paper, the ADI–FDTD is applied for the first time to imperfect guided-wave structures with walls of finite conductivities at microwave frequencies. It is incorporated with the unsplit PML [9] (that was shown to be equivalent to the split PML, but is more computationally efficient [10]). The simulations are performed for circular waveguides. Therefore, unlike the cases discussed by others [2], [3], [5]–[10], the effectiveness of the ADI–FDTD is tested in the nonrectangular coordinates that embody nonplane waves. Another point of significance is that fields, as well as their associated phenomena inside a highly conductive region, can now be simulated and, thus, visualized. This is not possible with the conventional FDTD or SIBC methods.

In the following sections, the formulations of the ADI–FDTD in the cylindrical coordinates with the unsplit PML implementation are presented for modeling open cylindrical structures. The numerical results are then shown with the computed attenuation constants, phase-shift constants, and surface impedance, as well as field distributions inside the conducting regions. Finally, conclusions and discussions are made.

II. Formulation of Cylindrical ADI–FDTD With the Unsplit PML Scheme for Conductive Media

The formulations of the ADI–FDTD method in cylindrical coordinates have been derived recently by the authors of [11]. To model highly conductive materials, the formulas need to be revised, and they were presented in [6]. Unlike from [6], the derivations here are carried out with the incorporation of the nonsplit uniaxial perfectly matched layer (UPML) boundary condition.

The derivations follow the similar procedure described in [11], but with the integration of the PML absorbing terms. Through some tedious mathematical manipulations, the unconditionally stable cylindrical ADI–FDTD algorithm can be obtained. For instance, (1a) and (1b), shown at the bottom of this page, can be found for the radial electrical field E_r in a UPML mediumfor the first half time step, see (2a) and (2b), shown at the bottom of the following page, for the second half time step, where

$$cr1\left(i+\frac{1}{2},j,k\right)=\kappa_r\left(i+\frac{1}{2},j,k\right)-\frac{\Delta t\cdot\sigma_r\left(i+\frac{1}{2},j,k\right)}{4\varepsilon}$$

$$cr2\left(i+\frac{1}{2},j,k\right)=\kappa_r\left(i+\frac{1}{2},j,k\right)+\frac{\Delta t\cdot\sigma_r\left(i+\frac{1}{2},j,k\right)}{4\varepsilon}$$

$$crI1\left(i+\frac{1}{2},j,k\right)=\kappa_r\left(i+\frac{1}{2},j,k\right)-\frac{\Delta t\cdot\int_{r_0}^{r}\sigma,(r)dr}{4\varepsilon}$$

$$crI2\left(i+\frac{1}{2},j,k\right)=\kappa_r\left(i+\frac{1}{2},j,k\right)+\frac{\Delta t\cdot\int_{r_0}^{r}\sigma_r(r)dr}{4\varepsilon}$$

$$cz1\left(i+\frac{1}{2},j,k\right)=\kappa_z\left(i+\frac{1}{2},j,k\right)+\frac{\Delta t\cdot\sigma_z\left(i+\frac{1}{2},j,k\right)}{4\varepsilon}$$

$$cz2\left(i+\frac{1}{2},j,k\right)=\kappa_z\left(i+\frac{1}{2},j,k\right)+\frac{\Delta t\cdot\sigma_z\left(i+\frac{1}{2},j,k\right)}{4\varepsilon}$$

$$cm\left(i+\frac{1}{2},j,k\right)=1+\frac{\Delta t\cdot\sigma\left(i+\frac{1}{2},j,k\right)}{2\varepsilon}. \tag{3}$$

$$\begin{aligned}
&E_r^{n+\frac{1}{2}}\left(i+\frac{1}{2},j,k\right)\\
&\quad=\frac{cz1\left(i+\frac{1}{2},j,k\right)E_r^n\left(i+\frac{1}{2},j,k\right)-cr1\left(i+\frac{1}{2},j,k\right)P_r^n\left(i+\frac{1}{2},j,k\right)}{cz2\left(i+\frac{1}{2},j,k\right)}\\
&\qquad+\frac{cr2\left(i+\frac{1}{2},j,k\right)\left[crI1\left(i+\frac{1}{2},j,k\right)P_r^n\left(i+\frac{1}{2},j,k\right)-P_r^n\left(i+\frac{1}{2},j,k\right)\right]}{cz2\left(i+\frac{1}{2},j,k\right)crI2\left(i+\frac{1}{2},j,k\right)}\\
&\qquad+\frac{cr2\left(i+\frac{1}{2},j,k\right)P_r^n\left(i+\frac{1}{2},j,k\right)}{cz2\left(i+\frac{1}{2},j,k\right)crI2\left(i+\frac{1}{2},j,k\right)cm\left(i+\frac{1}{2},j,k\right)}\\
&\qquad+\frac{\Delta t\cdot cr2\left(i+\frac{1}{2},j,k\right)}{2\varepsilon\cdot cz2\left(i+\frac{1}{2},j,k\right)crI2\left(i+\frac{1}{2},j,k\right)cm\left(i+\frac{1}{2},j,k\right)}\\
&\qquad\times\left[\frac{H_z^{n+\frac{1}{2}}\left(i+\frac{1}{2},j+\frac{1}{2},k\right)-H_z^{n+\frac{1}{2}}\left(i+\frac{1}{2},j-\frac{1}{2},k\right)}{\Delta\phi\cdot\left(i+\frac{1}{2}\right)\cdot r\left(i+\frac{1}{2}\right)}-\frac{H_\phi^n\left(i+\frac{1}{2},j,k+\frac{1}{2}\right)-H_\phi^n\left(i+\frac{1}{2},j,k-\frac{1}{2}\right)}{\Delta z\left(i+\frac{1}{2},j,k\right)}\right]
\end{aligned} \tag{1a}$$

$$\begin{aligned}
&P_r^{n+\frac{1}{2}}\left(i+\frac{1}{2},j,k\right)\\
&\quad=\frac{cr1(i+\frac{1}{2},j,k)}{cr2\left(i+\frac{1}{2},j,k\right)}P_r^n\left(i+\frac{1}{2},j,k\right)\\
&\qquad+\frac{1}{cr2\left(i+\frac{1}{2},j,k\right)}\left[cz2\left(i+\frac{1}{2},j,k\right)E_r^{n+\frac{1}{2}}\left(i+\frac{1}{2},j,k\right)-cz1\left(i+\frac{1}{2},j,k\right)E_r^n\left(i+\frac{1}{2},j,k\right)\right]\\
&P_r^{'n+\frac{1}{2}}\left(i+\frac{1}{2},j,k\right)\\
&\quad=P_r^{'n}\left(i+\frac{1}{2},j,k\right)+\left[crI2\left(i+\frac{1}{2},j,k\right)P_r^{n+\frac{1}{2}}\left(i+\frac{1}{2},j,k\right)-crI1\left(i+\frac{1}{2},j,k\right)P_r^n\left(i+\frac{1}{2},j,k\right)\right]
\end{aligned} \tag{1b}$$

Here, σ is the background electric conductivities of the medium, and $\sigma_d(d=r,z)$ is the directional conductivity in the direction in which the cylindrical waves are to be absorbed. P_r and P'_r are the auxiliary field components for the convenience of the computation.

Note that the lossy terms of the fields are not averaged in time, but using the most recent value of the electric field in computing conduction currents due to the effect of the threshold conductivity [12]. In addition, unlike originally presented in [13] for a PML, a nonunity term κ is introduced in the computation of cr or cz. κ can be considered as equivalent to the complex frequency shift of the complex frequency-shifted constitutive PML (CFS–PML) [8].

Although the above equations are for the radial field component, other field components and corresponding auxiliary components can be obtained in a similar way.

III. Numerical Experimetns

A. Numerical Validation of the Cylindrical UPML

The first step toward correct uses of the cylindrical UPML is to numerically validate it under the normal circumstance.

$$
\begin{aligned}
&E_r^{n+1}\left(i+\frac{1}{2},j,k\right)\\
&\quad=\frac{cz1\left(i+\frac{1}{2},j,k\right)E_r^{n+\frac{1}{2}}\left(i+\frac{1}{2},j,k\right)-cr1\left(i+\frac{1}{2},j,k\right)P_r^{n+\frac{1}{2}}\left(i+\frac{1}{2},j,k\right)}{cz2\left(i+\frac{1}{2},j,k\right)}\\
&\qquad+\frac{cr2\left(i+\frac{1}{2},j,k\right)\left[crI1\left(i+\frac{1}{2},j,k\right)P_r^{n+\frac{1}{2}}\left(i+\frac{1}{2},j,k\right)-P_r^{n+\frac{1}{2}}\left(i+\frac{1}{2},j,k\right)\right]}{cz2\left(i+\frac{1}{2},j,k\right)crI2\left(i+\frac{1}{2},j,k\right)}\\
&\qquad+\frac{cr2\left(i+\frac{1}{2},j,k\right)P_r'^{n+\frac{1}{2}}\left(i+\frac{1}{2},j,k\right)}{cz2\left(i+\frac{1}{2},j,k\right)crI2\left(i+\frac{1}{2},j,k\right)cm\left(i+\frac{1}{2},j,k\right)}\\
&\qquad+\frac{\Delta t\cdot cr2\left(i+\frac{1}{2},j,k\right)}{2\varepsilon\cdot cz2\left(i+\frac{1}{2},j,k,\right)crI2\left(i+\frac{1}{2},j,k,\right)cm\left(i+\frac{1}{2},j,k,\right)}\\
&\qquad\times\left[\frac{H_z^{n+\frac{1}{2}}\left(i+\frac{1}{2},j+\frac{1}{2},k\right)-H_z^{n+\frac{1}{2}}\left(i+\frac{1}{2},j-\frac{1}{2},k\right)}{\Delta\phi\cdot\left(i+\frac{1}{2}\right)\cdot r\left(i+\frac{1}{2}\right)}-\frac{H_\phi^n\left(i+\frac{1}{2},j,k+\frac{1}{2}\right)-H_\phi^n\left(i+\frac{1}{2},j,k-\frac{1}{2}\right)}{\Delta z\left(i+\frac{1}{2},j,k\right)}\right]
\end{aligned}
\tag{2a}
$$

$$
\begin{aligned}
&P_r^{n+1}\left(i+\frac{1}{2},j,k\right)\\
&\quad=\frac{cr1\left(i+\frac{1}{2},j,k\right)}{cr2\left(i+\frac{1}{2},j,k\right)}P_r^{n+\frac{1}{2}}\left(i+\frac{1}{2},j,k\right)\\
&\qquad+\frac{1}{cr2\left(i+\frac{1}{2},j,k\right)}\left[cz2\left(i+\frac{1}{2},j,k\right)E_r^{n+1}\left(i+\frac{1}{2},j,k\right)-cz1\left(i+\frac{1}{2},j,k\right)E_r^{n+\frac{1}{2}}\left(i+\frac{1}{2},j,k\right)\right]\\
&P_r'^{n+1}\left(i+\frac{1}{2},j,k\right)\\
&\quad=P_r'^{n+\frac{1}{2}}\left(i+\frac{1}{2},j,k\right)+\left[crI2\left(i+\frac{1}{2},j,k\right)P_r^{n+1}\left(i+\frac{1}{2},j,k\right)-crI1\left(i+\frac{1}{2},j,k\right)P_r^{n+\frac{1}{2}}\left(i+\frac{1}{2},j,k\right)\right]
\end{aligned}
\tag{2b}
$$

In doing so, we choose a circular waveguide with a radius of 5.0 mm to be the subject under study. The sidewall of the waveguide is a perfect conductor, while the two ends of the waveguide are terminated with the UPML layers. Based on the theory [14], the cutoff frequency for a certain mode should be

$$f_{c_{nm}} = \frac{P_{nm}}{2\pi a\sqrt{\mu\varepsilon}} \tag{4}$$

where p_{mn} is the mth root of the nth-order Bessel function $J_n(x)$ or its derivative, a is the radius, and μ and ε are the permeability and permittivity, respectively. Consider the TM_{01} mode for our investigation. The theoretical cutoff frequency is then 22.97 GHz.

The entire computation domain is now divided into three sections: the guided-wave section and the two UPML absorbing sections at the two ends of the guided-wave section. The directional conductivity of σ_z in the UPML section is determined by [15]

$$\sigma_z(z) = \sigma_{\max}\left(\frac{z}{\delta}\right)^m \tag{5}$$

where z is the distance from the air–UPML interface, δ is the thickness of the UPML layer, and $\sigma_{\max}$ is the maximum conductivity of the UPML layer. For the optimal performance, $\sigma_{\max}$ is recommended to be [15]

$$\sigma_{\max} = \sigma_{\mathrm{opt}} = \frac{m+1}{150\pi\sqrt{\varepsilon_r}\Delta z}. \tag{6}$$

In order to enhance the ability of absorbing the evanescent waves below the cutoff frequency, parameter κ_z is chosen from one to $\kappa_{\max}$ from the interface [15]. κ_z for each layer is

$$\kappa_z = 1 + \kappa_{\max}\left(\frac{z}{\delta}\right)^m. \tag{7}$$

To facilitate the comparisons with the theoretical solutions, the ADI–FDTD grid is excited with a modulated Gaussian pulse with the TM_{01} field spatial distributions. More specifically, the source function is

$$E_r = J_1(P_{nm}r)e^{-\left(\frac{t-t_0}{T}\right)^2}\cos(2\pi f_m t) \tag{8}$$

where J_1 is the first-order Bessel function, p_{nm} is the mth root of $J_1(x)$, r is the distance from the axis of the waveguide, t_0 is the time delay of the Gaussian pulse, and T is the width of the Gaussian pulse. f_m is the center frequency of the modulated Gaussian pulse. Based on [16], t_0 and T can be chosen with a desired frequency bandwidth. In other words, the source can be set up to contain substantial frequency components below cutoff frequency so that degrees of absorption of evanescent modes by the UPML can be observed.

The overall area is discretized into a grid of 10 (in r $\times$ 15 (in ϕ) $\times$ 60 (in z). The total length of the waveguide is 30 mm including the UPML layers. The time step was chosen to be equal to the CFL limit. The source plane is placed at the middle of the waveguide. It is a soft source and, therefore, the fields excited will propagate in both the $+z$- and $-z$-directions.

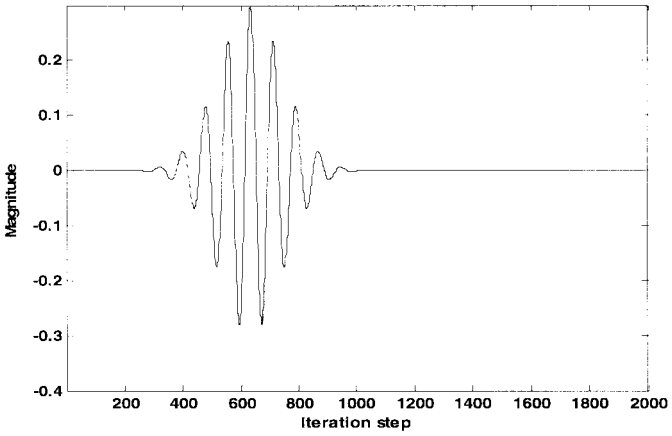

Fig. 1. E_r of 2000 iterations.

In summary, the parameters of the grid, the UPML layers, and the source are as follows:

$$\begin{aligned}
\Delta r &= 0.5 \text{ mm} \\
\Delta\phi &= 0.42 \text{ rad} \\
\Delta z &= 0.5 \text{ mm} \\
\Delta t &= 0.635 \text{ ps} \\
\sigma_{\max} &= 21.22 \text{ S/m} \\
\kappa_{\max} &= 20 \\
m &= 3.5 \\
t_0 &= 0.1 \text{ ns} \\
T &= 25 \text{ ps} \\
f_{\mathrm{in}} &= 40 \text{ GHz}.
\end{aligned} \tag{9}$$

Fig. 1 shows E_r with 2000 iterations at the grid point of $(1, 0, 30)$ (which is five cells away from the source plane and ten cells away from the PML). The waves in the waveguide die down after 1000 iterations, which indicates that the waves are absorbed well by the UPML layers. To obtain the quantitative measurements of the reflections, a reference simulation of a long waveguide section of 400 Δz was first run. The simulated E_r was recorded as the incident wave. The reflection coefficient for the PMLs was then calculated with $|E_{r(\text{with PMLs})} - E_{r(\text{long section})}|/|E_{r(\text{long section})}|$. Fig. 2 shows the reflection coefficients in the frequency domain. The PML absorptions are observed better than -50 dB in most cases, even below cutoff. Therefore, we conclude that the UPML with the addition of nonunity κ is very effective in absorbing cylindrical waves that include the evanescent modes.

B. Computation of the Waveguide With Highly Conductive Wall

In this section, we will show that the ADI–FDTD method combined with the cylindrical UPML boundary conditions is effective for simulating the open structures containing conductive materials. Since few results are reported for exact computations of the cylindrical waveguide with a wall of finite conductivity,

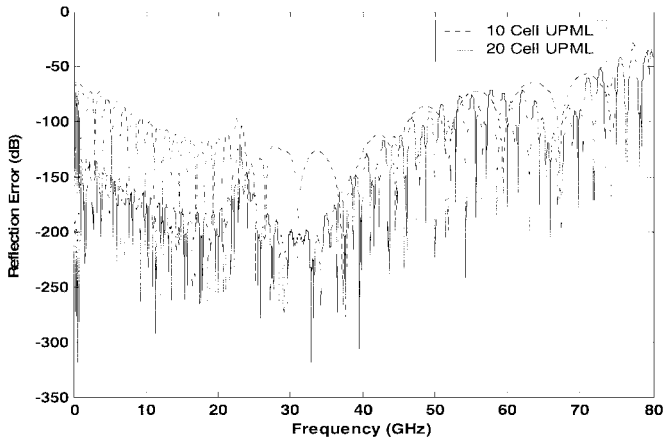

Fig. 2. Numerical reflections from the UPML layers.

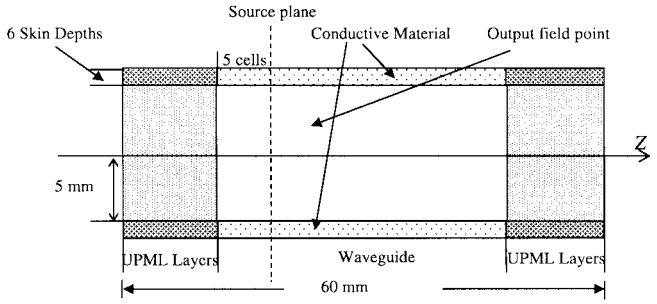

Fig. 3. Nonperfect waveguide under study.

two additional sets of simulations with other methods were also run and compared with the ADI–FDTD simulations. One is the conventional FDTD method and the other one is the approximate SIBC approach [17] (that is widely used for treating highly conductive materials with FDTD thus far).

Consider the circular waveguide, as described in the previous subsection, but with a wall of a finite conductivity this time (see Fig. 3). The meshing method is similar to the one used in [6]. In the radial direction r, gradually decreased cell sizes were applied to the air-filled area, and a fine uniform grid was used inside the conducting wall. The largest size $\Delta r_{\max}$ is 0.625 mm, while the smallest size $\Delta r_{\min}$ (which is the cell size inside the conducting wall) was chosen to be one-third of skin depth. For copper, $\Delta r_{\min} = 9.54$ nm at 40 GHz. Therefore, the cell size ratio of the largest cell size to the smallest cell size is as large as 65 513 in the r-direction at 40 GHz. In the azimuthal direction and z-direction, uniform discretization was applied with $\Delta\phi = 0.42$ rad and $\Delta z = 0.5$ mm. Overall, a $39 \times 15 \times 120$ mesh is generated for the whole computation domain. The thickness of the conductive wall is taken to be approximately six times the skin depth, long enough for the fields to decay to a negligible level. Other simulation parameters remain the same as those used in Section III-A.

The first two parameters under study are attenuation constant α and phase-shift constant β. The parameters were computed via

$$\alpha = -\frac{1}{h} ln \left| \frac{\Im\big(E_r(z+h,t)\big)}{\Im\big(E_r(z,t)\big)} \right| \tag{10}$$

$$\beta = \frac{1}{h} \mathrm{Im} \left| ln \frac{\Im\big(E_r(z,t)\big)}{\Im\big(E_r(z+h,t)\big)} \right| \tag{11}$$

where $\Im$ represents the Fourier transform at a selected frequency. z is taken to be at 10 Δz away from the source, and the distance h is 10 Δz. Im is the operator that takes the imaginary part of a complex variable.

Tables I and II show the computed attenuation and phase-shift constants with different conductivities using different methods. In them, quantity p is introduced to represent the degree of conductivity of the walls as follows:

$$p = \frac{\sigma}{\omega\varepsilon}. \tag{12}$$

The higher value of p, the higher conductive degree of the wall. In our simulations, p varies from 10 to 10^5 and 2.62×10^7. It corresponds to the conductivity of the wall varying from 22.22 to 22 222.22 (s/m) and 5.8×10^7 s/m (for copper) at 40 GHz. From Tables I and II, the following observations can be made.

1) The results obtained with the FDTD and ADI–FDTD methods are very close to each other, and the differences are less than 0.5%. Since the FDTD is a well-proven method, we conclude that the ADI–FDTD method is valid and effective in computing conductive media, regardless of the values of conductivities. In other words, the accuracy of the ADI–FDTD method is at the same level as that of the FDTD method. The ADI–FDTD method can be a substitute for the conventional FDTD method whenever applicable
2) There exist differences between the results obtained with the SIBC method and those obtained with the FDTD or ADI–FDTD methods. The smaller the p value, the larger the differences. That means that when the wall becomes less conductive, the SIBC method becomes less accurate. The reason is that the SIBC method is assumed of plane-wave propagation in a conductive medium. In a medium of low or medium–high conductivities $(p = 10 - 10\,000)$ or cylindrical structures, the assumption is no longer valid. Therefore, the results obtained with the SIBC approach will be quite different and most likely inaccurate.
3) The phase-shift constants do not change much with variations of the conductivities, while the attenuation constants do. This reflects the fact that the variations of the wall conductivity have more impact on the attenuation constant of the fields than that on the phase-shift constant, as the energy is absorbed by the lossy wall.

Note that, in the above computations, the FDTD method is used for the purpose of validating the ADI–FDTD method. The computation time required for the FDTD simulations is much higher than that for the ADI–FDTD method because of the CFL stability condition. In fact, for the case of the copper wall, the FDTD computation time became so high that we were not able to complete the FDTD simulation in days (this is why in Tables I and II, no results are shown with the FDTD method for the copper case). Table III gives the comparison of the time used by the FDTD and ADI–FDTD methods. As can been seen from Table III, for the FDTD method, the total simulation time

TABLE I
COMPUTED ATTENUATION CONSTANTS WITH DIFFERENT CONDUCTIVITIES

p	Attenuation constant (Nepers/m)				
	SIBC	ADI-FDTD	FDTD	Difference between FDTD and (%):	
				SIBC	ADI-FDTD
10	29.47	70.56	70.33	-58.10	+0.33
100	9.21	18.87	18.80	-51.01	+0.37
1000	3.02	5.79	5.78	-47.75	+0.17
10000	1.00	1.81	1.83	-45.36	-1.09
2.62×10^7 (copper)	0.0136	0.1012	N/A	N/A	N/A

TABLE II
COMPUTED PHASE SHIFT CONSTANTS WITH DIFFERENT CONDUCTIVITIES

p	Phase shift constant (radian/m)				
	SIBC	ADI-FDTD	FDTD	Difference between FDTD and (%):	
				SIBC	ADI-FDTD
10	685.91	698.13	698.13	-1.75	0
100	685.91	698.13	698.13	-1.75	0
1000	685.91	698.13	698.13	-1.75	0
10000	685.91	698.13	698.13	-1.75	0
2.62×10^7 (copper)	685.91	687.33	N/A	N/A	N/A

TABLE III
COMPUTATION TIME BY THE FDTD AND ADI–FDTD METHODS

p	Time step Δt (ps)			Simulation time T (s)		
	FDTD	ADI-FDTD	Ratio	FDTD	ADI-FDTD	Ratio
10	0.103	0.635	6.17	916.91	1329.98	0.69
100	3.25×10^{-2}	0.635	19.54	4791.95	1467.19	3.27
1000	1.03×10^{-2}	0.635	61.65	8724.17	1549.83	5.63
10000	3.25×10^{-3}	0.635	195.38	31905.17	1637.13	19.49

TABLE IV
MEMORY USAGE BY THE FDTD AND ADI–FDTD METHODS

p	FDTD (Mbytes)	ADI-FDTD (Mbytes)
10	12.6	27.1
100	13.1	29.5
1000	14.1	30.8
10000	15.6	32.1

(T) tends to increase with higher conductivity because of the smaller time step. For the ADI–FDTD method, the total simulation time just slightly increases with higher conductivity. Consequently, the higher the conductivity, the larger savings with the ADI–FDTD method in simulation run time. When p is larger than 10 000, the saving is more than 19 times.

Table IV shows the memory used by the FDTD and ADI–FDTD methods. The ADI–FDTD method requires about double the amount of memory required by the FDTD method due to the fact that more field components at each time step are computed with the ADI–FDTD. The detailed explanations were offered in [2] and [3].

To shed more light on the accuracy of the ADI–FDTD method (which can now be considered to produce the solutions almost the same as those from the FDTD method), Fig. 4 shows the wave impedance in the air-filled region with different conductivities in comparisons with the theoretical solutions. The theoretical impedance value is the wave impedance with a perfect conducting wall. As can be seen, the higher the p value, the closer the impedance computed with the ADI–FDTD method is to the theoretical value with a perfect electric conductor (PEC). Consequently, the results obtained with the ADI–FDTD method are reasonably accurate. Ripples are observed at the higher end of the frequency range. We cannot identify the exact cause. Our

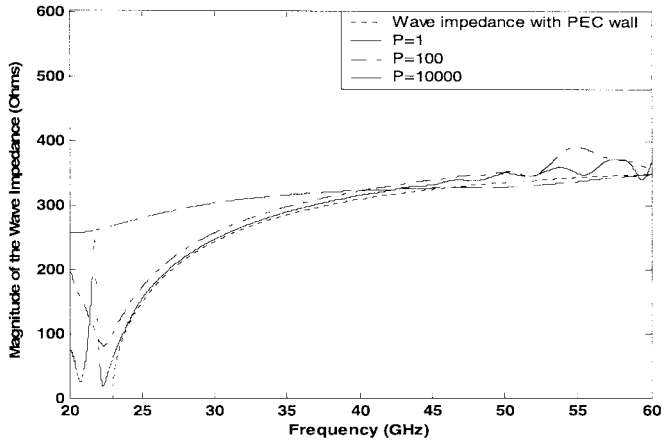

Fig. 4. z-directed wave impedance in the air-filled area with different conductivities.

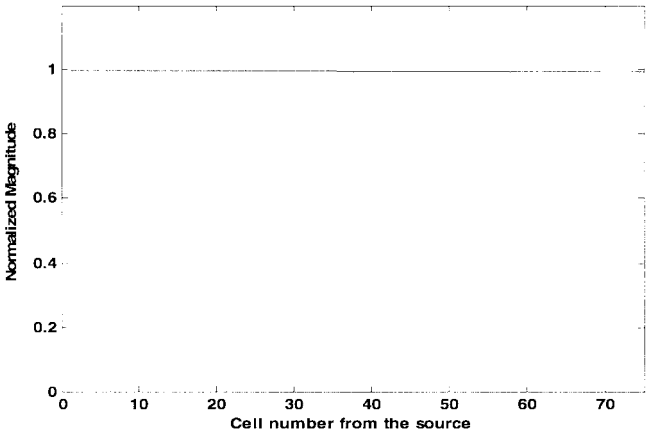

Fig. 5. Field attenuation along the propagation direction.

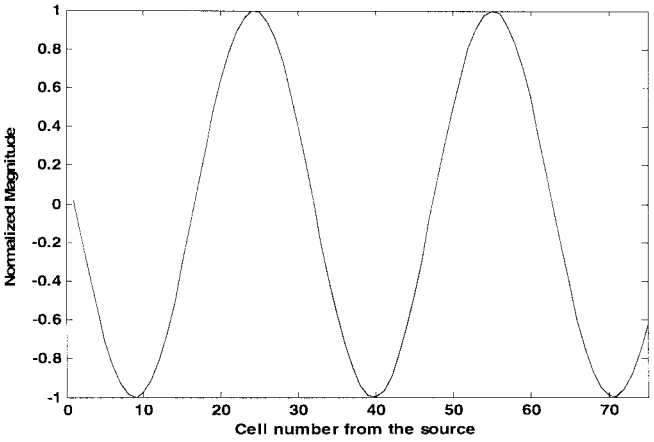

Fig. 6. Snap shot of the E_r distribution in the z-direction.

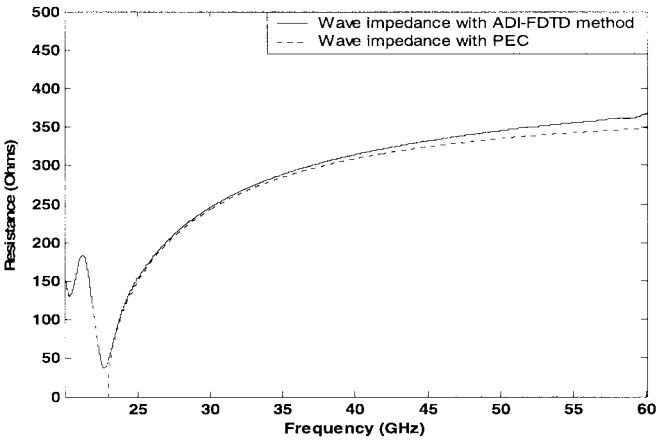

Fig. 7. Wave impedance in the air-filled area.

conjecture is that they are due to the dispersion error of the ADI–FDTD method in a conducting medium at high frequencies. Further investigation along this line is currently under way.

C. Computation of the Waveguide With Copper Wall

Thus far, we have shown that the ADI–FDTD method can achieve the same accuracy as the FDTD method with much less computation time in modeling conductive media. We then applied the ADI-FDD method to the copper wall, which is more of a realistic problem.

The computed attenuation and phase-shift constants were already shown in Table I and II. The phase-shift constant is very close to an analytical solution with the perfect wall. The attenuation constants are, however, different from those obtained with the SIBC approach. Since the ADI–FDTD method has previously proven to be in a consistent agreement with the FDTD method, more confidence should be given to the ADI–FDTD results than to the SIBC results.

Below, other results, namely, field distributions and wave impedances, are shown. These results are presented simply because they can demonstrate that ADI–FDTD method not only has the normal capability of the conventional FDTD and SIBC methods, but also the capability that the two methods do not have.

1) Field Distributions and Wave Impedance in the Air-Filled Region: Fig. 5 shows the field attenuation along the z-direction computed with the ADI–FDTD method, while Fig. 6 is a snap shot of E_r at 40 GHz with the ADI–FDTD method. From these two figures, one can see that the ADI–FDTD method does pick up the field attenuation, even it is small (as expected, due to high conductivity of copper).

Fig. 7 shows that the magnitude of the z-directed wave impedance simulated with the ADI–FDTD method, as well as the analytical results with the assumption of the PEC wall. The impedance is computed with the following equation:

$$Z_{\text{air z-directed}} = \left| \frac{\Im\big(E_r(z,t)\big)}{\Im\big(H_\phi(z,t)\big)} \right|. \tag{13}$$

As can be seen, impedance calculated with the ADI–FDTD method is very close to the theoretical result with the PEC wall. The ripples at the very low frequencies may be attributed to the computer roundoff errors since the field intensities below the cutoff frequency attenuate so much at the output points that the roundoff errors simply override the real field values of small values below cutoff.

2) Field Distributions and Wave Impedance in the Conducting Wall: Unlike the SIBC method, which cannot provide information on field distributions in the conductive region, the ADI–FDTD method is capable of simulating fields inside

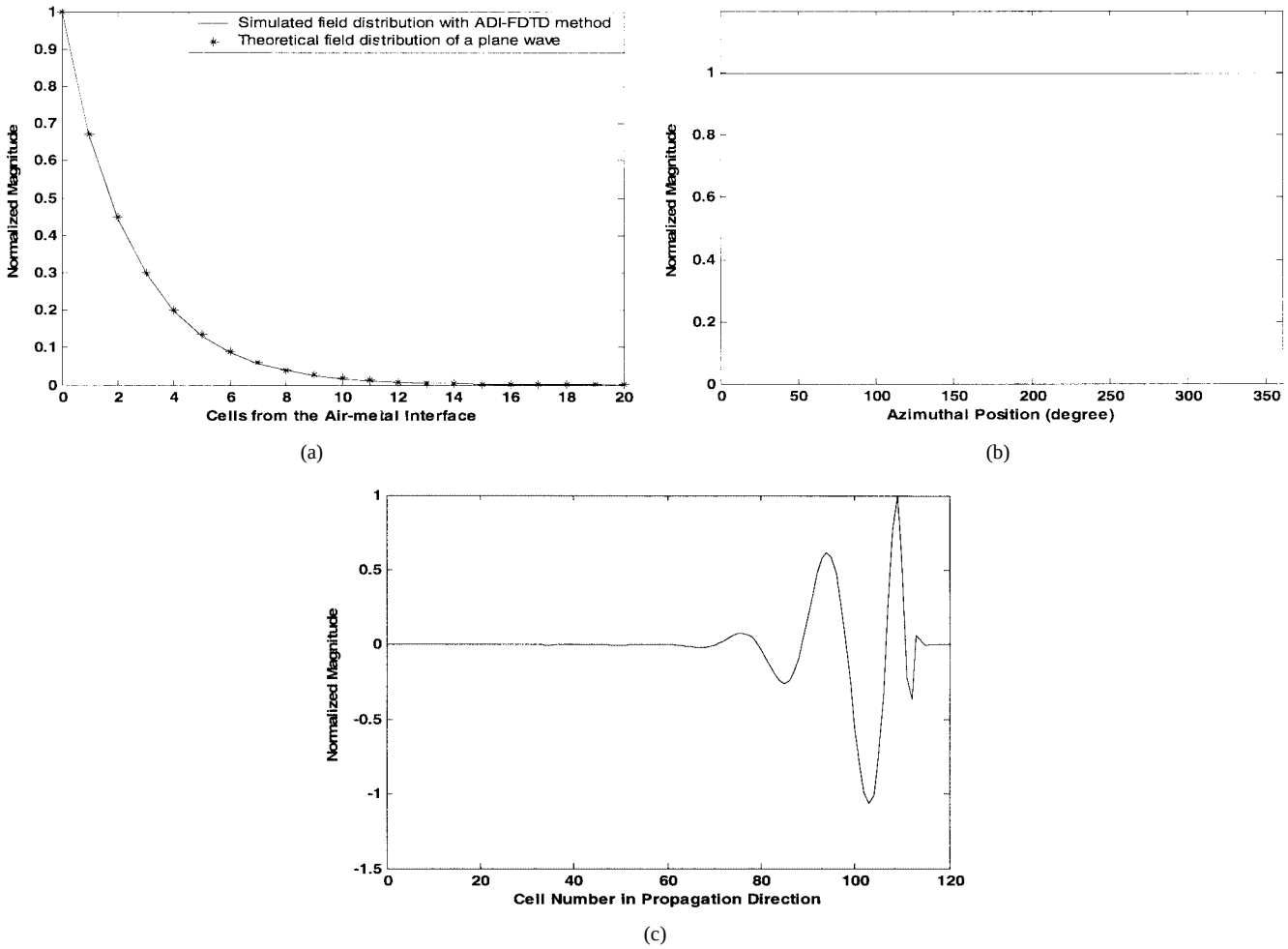

Fig. 8. (a) Field distribution in the conductive region in the radial direction at 40 GHz. (b) Field distribution in the conductive region in the azimuthal direction at 40 GHz. (c) Field distribution in the conductive region in the propagation direction.

the conductive region. By recording time-domain field values at each grid point along a direction inside the wall, field distributions, as well as the impedance in that direction can be obtained. Fig. 8(a)–(c) shows the field distribution inside the conductive region along the three respective directions.

From Fig. 8(a), one can see that the field is attenuated in the radial direction. The theoretical distribution comes from the well-known case of the plane-wave propagation in a conducting medium documented in most textbooks (where the field is attenuated with $e^{-r/\delta}$, with δ being the skin depth). The simulated and theoretical field distributions are close to each other. It means that, for highly conductive media, the field is attenuated as it is for a plane-wave situation. However, this does not mean that the fields inside the conducting wall can be treated like a plane wave since the fields are distributed differently in the other directions. In the azimuthal and longitudinal directions [see Fig. 8(b) and (c)], the fields are not attenuated with the factor of $e^{-r/\delta}$. Rather, they vary with the cylindrical mode field distributions like those in the air region. In our case, fields do not vary in the azimuthal direction, but propagate in the longitudinal direction.

In correspondence to the field variations in the three directions inside the copper region, wave impedances on the surface of the copper wall along the three directions were also computed via the following equations:

$$Z_r = \left| \frac{\Im\big(E_z(z,t)\big)}{\Im\big(H_\phi(z,t)\big)} \right|$$
$$Z_\phi = \left| \frac{\Im\big(E_z(z,t)\big)}{\Im\big(H_r(z,t)\big)} \right|$$
$$Z_z = \left| \frac{\Im\big(E_r(z,t)\big)}{\Im\big(H_\phi(z,t)\big)} \right|. \tag{14}$$

Fig. 9 shows the computed results. Particular attention should be paid to the impedance in the radial direction shown in Fig. 9(a). It represents the surface impedance of the copper wall. As a reference, the surface impedance used with the SIBC approach is also shown in Fig. 9(a). As seen, both impedances are close to each other, especially in a lower frequency range where p is larger. This validates the SIBC approach for modeling of highly conductive materials that are represented by large p. The impedances shown in Fig. 9(b) and (c), however, are not associated with the surface impedance, but with the mode impedances. The z-directed wave impedance has a dip that corresponds to the cutoff frequency. To the authors' best knowledge, values of these impedances in conducting media

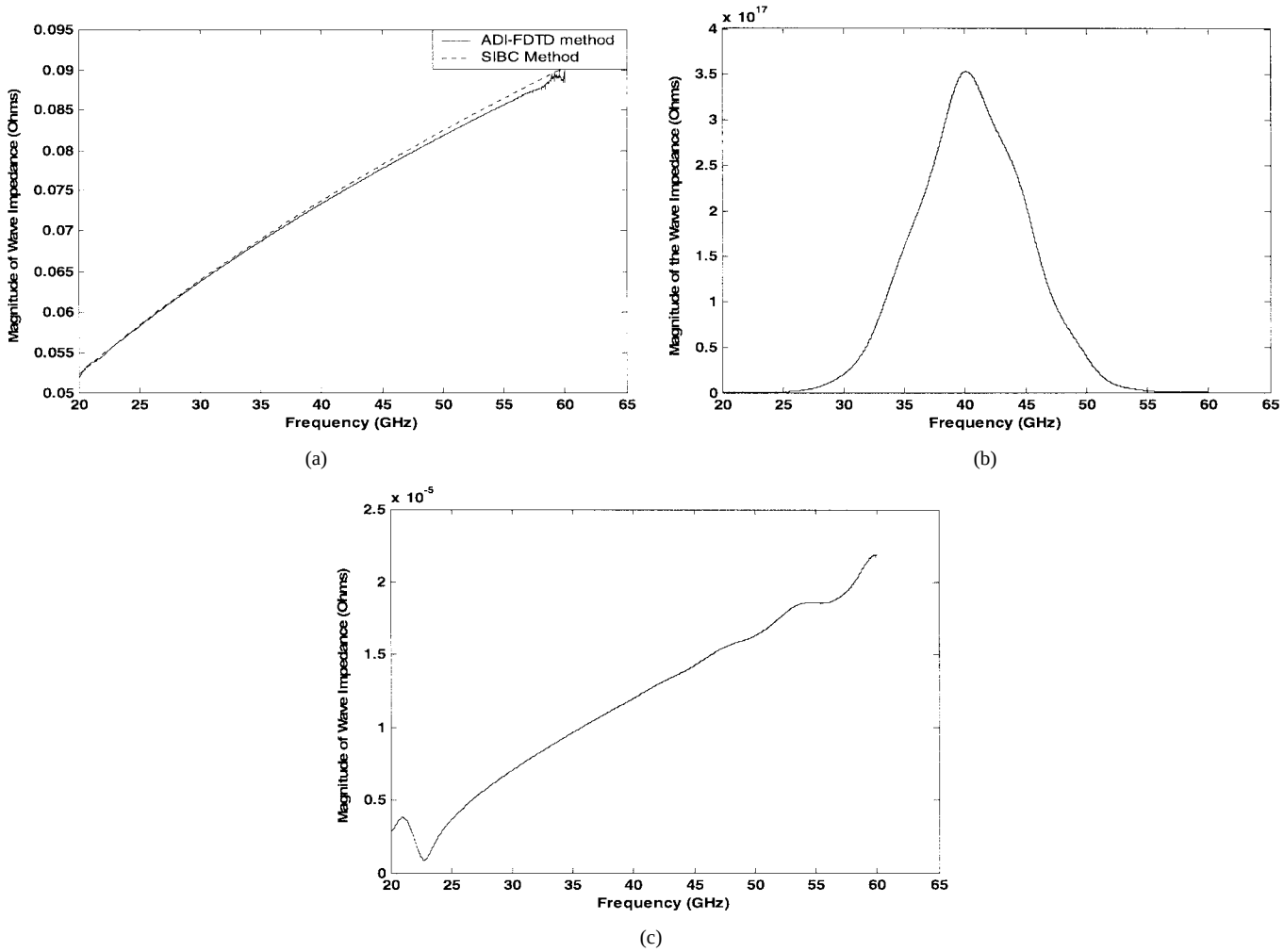

(a) (b) (c)

Fig. 9. (a) Wave impedance in the radial direction in the conductive area. (b) Wave impedance in the azimuthal direction in the conductive area. (c) Wave impedance in the propagation direction in the conductive area.

have not been reported thus far in literature. This paper, for the first time, presents the results. This is significant in modeling of the highly conductive media with methods of FDTD types.

IV. Conclusions

In this paper, extensive investigations on the application of the ADI–FDTD method to modeling of conductive materials has been presented. Also, the unsplit PML was implemented into the cylindrical ADI–FDTD method for simulating open structures that contain conductive medium. Our studies show the following.

1) The ADI–FDTD method can generate the results that are almost the same as those with the conventional FDTD method, but with much less computation time for highly conductive materials. In the case of highly conductive walls, such as copper walls, the computation time is comfortably manageable with the ADI–FDTD method, but becomes prohibitorily large with the conventional FDTD method. In other words, the ADI–FDTD method can be an effective substitute for the conventional FDTD method whenever the conventional FDTD method is not practically applicable,
2) Both the ADI–FDTD and the SIBC methods can effectively handle highly conductive materials. Although the SIBC method renders saving in computation expenditure (since it does not require meshing within conductive regions), the ADI–FDTD method is capable of simulating the fields inside the conductive regions. For conducting media of low to medium–high conductivities, the SIBC method does not provide solutions with good accuracies, while the conventional FDTD method requires larger CPU time than the ADI–FDTD method.

In conclusion, the ADI–FDTD method can serve as an effective universal tool for modeling of conductive media, regardless of the degrees of medium conductivity. The main reason is that it does not have the CFL condition that restricts its time step from being a large value, even when the modeling accuracy is adequate.

References

[1] A. Taflove, *Computational Electrodynamics: The Finite-Difference Time-Domain Method*. Boston, MA: Artech House, 1995.
[2] F. Zhen, Z. Chen, and J. Zhang, "Toward the development of a three-dimensional unconditionally stable finite-difference time-domain method," *IEEE Trans. Microwave Theory Tech.*, vol. 48, pp. 1550–1558, Sept. 2000.

[3] T. Namsiki, "3-D ADI–FDTD method-unconditionally stable time-domain algorithm for solving full vector Maxwell's equations," *IEEE Trans. Microwave Theory Tech.*, vol. 48, pp. 1743–1748, Oct. 2000.
[4] F. Zheng and Z. Chen, "Numerical dispersion analysis of the unconditionally stable 3-D ADI–FDTD method," *IEEE Trans. Microwave Theory Tech.*, vol. 49, pp. 1006–1009, May 2001.
[5] T. Namiki and K. Itoh, "Numerical simulation using ADI–FDTD to estimate shielding effectiveness of thin conductive enclosures," *IEEE Trans. Microwave Theory Tech.*, pp. 1060–1066, June 2001.
[6] C. Yuan and Z. Chen, "Towards accurate time-domain simulation of highly conductive materials," in *IEEE MTT-S Int. Microwave Symp. Dig.*, Seattle, WA, June 2002, pp. 1335–1338.
[7] J. P. Berenger, "A perfectly matched layer for the absorption of electromagnetic waves," *J. Comput. Phys.*, vol. 114, pp. 185–200, 1994.
[8] ——, "An efficient FDTD implementation of the PML with CFS in general media," in *IEEE AP-S Int. Symp.*, vol. 3, 2000, pp. 1362–1365.
[9] J. A. Roden and S. D. Gedney, "Efficient implementation of the uniaxial-based PML media in three-dimensional nonorthogonal coordinates with the use of FDTD technique," *Microwave Opt. Technol. Lett.*, vol. 14, no. 2, pp. 71–75, Feb. 1997.
[10] J.-P. Berenger, "Numerical reflection from FDTD-PMLs: A comparison of the split PML with the unsplit PML and CFS PMLs," *IEEE Trans. Antennas Propagat.*, vol. 50, pp. 258–265, Mar. 2002.
[11] C. Yuan and Z. Chen, "A three dimensional unconditionally stable ADI–FDTD method in the cylindrical coordinate system," *IEEE Trans. Microwave Theory Tech.*, vol. 50, pp. 2401–2405, Oct. 2002.
[12] R. J. Lubbers, F. Hunsberger, and K. S. Kunz, "Modeling good conductors using the finite-difference time-domain technique," *IEEE Trans. Electromagn. Compat.*, vol. 37, pp. 210–216, May 1995.
[13] W. C. Chew and W. H. Weedon, "A 3-D perfectly matched medium from modified Maxwell's equations with stretched coordinates," *Microwave Opt. Technol. Lett.*, vol. 7, no. 13, pp. 599–603, Sept. 1994.
[14] M. Pozar, *Microwave Engineering*. Reading, MA: Addison-Wesley, 1990.
[15] A. Taflove, *Advances in Computational Electrodynamics: The Finite-Difference Time-Domain Method*. Norwood, MA: Artech House, 1998.
[16] C.-S. Shin and R. Nevels, "Optimizing the Gaussian excitation function in the finite difference time domain method," *IEEE Trans. Educ.*, vol. 45, pp. 15–18, Feb. 2002.
[17] C. Wang, B. Q. Gao, and C. P. Deng, "Accurate study of Q-factor of resonator by a finite-difference time-domain method," *IEEE Trans. Microwave Theory Tech.*, vol. 43, pp. 1524–1529, July 1995.

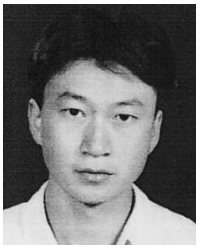

Chenghao Yuan (S'00) received the B.Eng. degree from Xidian University, Xi'an, China, in 1995, the M.A.Sc. degree from Tianjin University, Tianjin, China, in 1998, and is currently working toward the Ph.D. degree at Dalhousie University, Halifax, NS, Canada.

His research interests include computational electromagnetics, RF circuit design, numerical modeling of multilayer thin-film structures, and wireless communication system design.

Zhizhang (David) Chen (S'92–M'92–SM'96) received the B.Eng. degree from Fuzhou University, Fuzhou, China, in 1982, the M.A.Sc. degree from Southeast University, Nanjing, China, in 1986, and the Ph.D. degree from the University of Ottawa, Ottawa, ON, Canada, in 1992.

From January of 1993 to August of 1993, he was a Natural Science and Engineering Research Council Post-Doctoral Fellow with the Department of Electrical and Computer Engineering, McGill University, Montreal, QC, Canada. In 1993, he joined the Department of Electrical and Computer Engineering, DalTech, Dalhousie University, Halifax, NS, Canada, where he is currently a Professor. He has authored and coauthored over 100 journal and conference papers, as well as industrial reports in the areas of computational electromagnetics and RF/microwave electronics for wireless communications. His current research interests include RF/microwave electronics, numerical modeling and simulation, and antenna designs for wireless and satellite communications.